Tellurium self-diffusion in amorphous Ge2Sb2Te5 phase change materials

Qingmei Gong, Haihong Jiang, Jacques Perrin-Toinin, Martin Peterlechner, Magali Putero, Alain Portavoce, Sergiy Divinski, Gerhard Wilde

Published in Acta Materialia (2023) https://doi.org/10.1016/j.actamat.2023.119146

Tellurium self-diffusion in amorphous $Ge_2Sb_2Te_5$ phase change materials

Qingmei Gong[1], Haihong Jiang[1], Jacques Perrin-Toinin[2], Martin Peterlechner[1,3], Magali Putero[2], Alain Portavoce[2], Sergiy Divinski[1], Gerhard Wilde[1]

[1]*Institute of Materials Physics, University of Münster, Wilhelm-Klemm-Str. 10, 48149 Münster, Germany*

[2]*IM2NP, Faculté des Sciences et Techniques, 13397 Marseille, France*

[3]*Laboratory for Electron Microscopy, Karlsruhe Institute for Technology, Engesserstr. 7, D-76131 Karlsruhe, Germany*

Abstract

Amorphous $Ge_2Sb_2Te_5$ phase change material is considered as a prototype material for non-volatile memories due to the reversibility of the amorphous-to-crystalline transition on a nanosecond timescale. In this context, the kinetics of atomic self-diffusion has important bearings for the crystallization process and the switching behavior of phase change materials. It is thus important for applications as well as for the general understanding of the rapid and reversible switching behavior to understand atomic self-diffusion, especially in the amorphous phase. However, up to now, reliable data on the kinetics of atomic self-diffusion in amorphous phase change materials is almost non-existent. For this reason, Te tracer diffusion was measured using secondary ion mass spectroscopy and applying the highly enriched natural ^{122}Te isotope. For the first time, Te self-diffusion coefficients in amorphous $Ge_2Sb_2Te_5$ are experimentally measured and the activation energy of Te self-diffusion was determined as (1.43 ± 0.08) eV.

Keywords: Phase change materials, $Ge_2Sb_2Te_5$, diffusion, amorphous

1. Introduction

Phase change materials (PCMs) have attracted much attention over the past decades due to their promising application in rewritable and non-volatile phase change memory (PCM) devices [1–3]. More than four orders of magnitude electrical contrast and a tremendous difference in optical properties between the amorphous (high resistance) and crystalline (low resistance) phases enable PCM technology to read, write, and store digital data [4–7]. The basis of these functions is directly related to the reversibility of the amorphous-to-crystalline transition that proceeds on a nanosecond timescale. This has been recognized as early as 1968 by Ovshinsky in the study of electrical switching [8]. This operation requires PCMs to be repeatedly heated, melted and vitrified by optical or electrical pulses to induce the respective phase transformations, i.e. crystallization, melting or glass formation. The processes of amorphization and crystallization are accompanied by atomic displacements and segregation which may lead to reliability issues and can cause early cell failure during device operation because of the compositional variations [9–12]. Operating temperatures as high as 85°C in embedded memory devices or even as high as 150°C for automotive applications enhances the atomic transport [13–15]. Atomic diffusion can influence the crystallization process and the switching behavior of PCMs. Hence, to ensure the success of PCM technology in data storage industries, it is a crucial issue to understand the atomic diffusion, especially in the amorphous phase.

Among prevailing PCMs, even though the prototypical PCM $Ge_2Sb_2Te_5$ (GST) has gained the most attention, and has already been successfully applied in optical and electrical

storage devices including Blu-ray- and DVD-rewritable discs [16–19] owing to the pioneering work of Yamada et al [20–22], reliable experimental data related to self-diffusion in such materials are very limited. In the literature, some diffusion parameters in molten and crystalline GST were reported [23–26]. At high temperatures above the melting point, T_m, the Stokes-Einstein relation between diffusivity and viscosity is often applied to evaluate the atomic mobility parameters, nevertheless, this relationship will break down when the temperature decreases below $1.2T_g$ due to heterogeneous and cooperative dynamics [23–25] (here T_g is the glass transition temperature). Yang et al. [26] studied the composition variation in an electrical field driven by electrostatic force-induced electromigration. An effective diffusion coefficient of Te in the crystalline phases was estimated to be about 10^{-18} m^2/s at 433 K by calculating the product of the diffusion coefficient and the effective charge of constituent atoms. However, to the best of our knowledge, self-diffusion in amorphous PCMs has not yet been measured. The lack of reliable diffusion data for amorphous GST is primarily attributed to its metastability [27,28]. The fast crystallization and the comparatively low crystallization temperature (150°C) have posed significant challenges for studying diffusion in the amorphous state, which demands that diffusion experiments have to be accomplished at low temperatures and short times. In addition, below the crystallization temperature, the high energies of covalent bonds prevailing in amorphous PCMs result in low self-diffusion rates [29]. The resulting small diffusion lengths in the nanometer range and low diffusion coefficients, about 10^{-24} m^2/s, require the usage of high-sensitivity detection techniques. These serious complications limit diffusion studies on such amorphous materials.

The fundamental diffusion data are of high importance for amorphous PCMs, especially with respect to their thermal stability and service lifetimes. Furthermore, reliable self-diffusion data allow optimizing the crystallization behavior and assessing a complete description of the kinetics of the phase transformations. For all these reasons, the present study is focused on experimental measurements of Te tracer diffusion in the amorphous phase change material $Ge_2Sb_2Te_5$.

2. Experimental details

2.1 Synthesis of GST thin films

Amorphous GST thin films were produced via DC magnetron sputter deposition using a stoichiometric target (2 inches in diameter) at room temperature (RT). Single-crystal silicon wafers of (100) orientation were used as substrates, which were pre-cleaned by acetone and distilled water. The base pressure of the sputter system was below 10^{-8} mbar. An Ar pressure of 5×10^{-3} mbar and 30 W applied power were used to deposit the films. All sputtering parameters were chosen to provide the best quality films, and 200 nm thick samples were finally fabricated by adjusting the deposition time. The thickness of all samples was determined by a profilometer (DektakXT from Bruker).

For transmission electron microscopy (TEM) characterization, cross-sectional TEM lamellae of the ^{122}Te/GST diffusion samples were prepared by focused ion beam (FIB) sputtering using a Zeiss CrossBeam 340. Sample transfer was accomplished using a glovebox with Ar-atmosphere and a Gatan vacuum transfer holder. For TEM, a Titan Themis G3 300 TEM (FEI) was used at 300 kV applying conventional TEM and scanning-TEM (STEM). Chemical analysis was made by energy-dispersive X-ray spectroscopy (EDS) in STEM mode using all 4

EDS detectors of the ChemiSTEM system. Moreover, nanobeam diffraction patterns (NBDPs) were acquired using the μProbe-mode to obtain a 1 nm spot with only 1 mrad convergence angle.

2.2 Alloy characterization

The structural characterization was carried out using X-ray diffraction (XRD, Siemens D5000) and high-resolution transmission electron microscopy (HR-TEM, Thermo Fisher FEI Themis G3 60-300) measurements. All XRD data were collected at room temperature using Cu-Kα radiation (λ = 1.5406 Å) in the 2θ angular range of 20°- 80° with a step size of 0.02°. Non-contact atomic force microscopy (AFM, Park XE-100) was applied to image the surface topography of the thin films on the atomic scale. Scans of a 15×15μm^2 area were performed with NSC15 uncoated Si tips with a typical radius of 8 nm.

Additionally, chemical analysis of the films was performed by STEM coupled with an EDS detector (FEI Chemistem™). Furthermore, the composition was also checked by atom probe tomography (APT) using a CAMECA LEAP 3000X-HR system. The APT samples were prepared by a FIB FEI Helios 600 NanoLab using the standard procedure as described in [30]. The measurements were performed in the laser mode at $T \sim 50$ K with a laser energy of 0.5 nJ, a laser pulse frequency of 100 kHz, and an average detection rate of 2 ions per 1000 laser pulses. Finally, the data were processed with the IVAS 3.6.14 software.

2.3 Tracer diffusion measurements

The stable ^{122}Te isotope and GST thin films with a thickness of about 200 nm were utilized for the current diffusion measurements. A thin layer of a highly-enriched (to 98%) ^{122}Te isotope (natural abundance of 2.55%) was deposited on the surface of the as-deposited GST film using physical vapor deposition (PVD) under a vacuum condition lower than 10^{-5} mbar. The mass gain, due to ^{122}Te deposition, was determined by weighing the sample using a microbalance (Sartorius Supermicro S4) with a resolution of 0.1 μg and taking the differences of the sample masses before and after the ^{122}Te deposition process, $\Delta m = m_2 - m_1$. Knowing the theoretical density, ρ, and the deposition area, s, an average thickness, $\bar{h}$, of the ^{122}Te layer of about 16 nm was estimated as

$$\bar{h} = \frac{\Delta m}{\rho s} \qquad (1)$$

To precisely determine the ^{122}Te thickness, a mask was used during the ^{122}Te deposition as shown in Fig. 1(a), then profilometry was applied, see the results in Fig. 1(b). In the entire area, the ^{122}Te thickness varied in the range of 14-30 nm, which was determined by more than 25 measurements along the *y* axis, as shown in Fig. 1(c). The dashed line indicates the average thickness of 19 nm obtained by profilometry. As a result, a reasonably flat and dense tracer layer was prepared, taking into account the size of the inspected areas during the time-of-flight secondary ion mass spectrometry (ToF-SIMS) profiling, see below. The minor difference between the estimated and measured layer thickness can be explained by a reduced density of the deposited ^{122}Te layer that does not affect the performed tracer diffusion measurements.

Subsequently, diffusion annealing treatments were carried out in a sealed aluminum tube under highly purified Ar atmosphere using an oil bath. In order to avoid the onset of crystallization at higher temperatures, the present measurements were carried out below the glass transition temperature (T_g). The annealing times and temperatures are listed in Table 1.

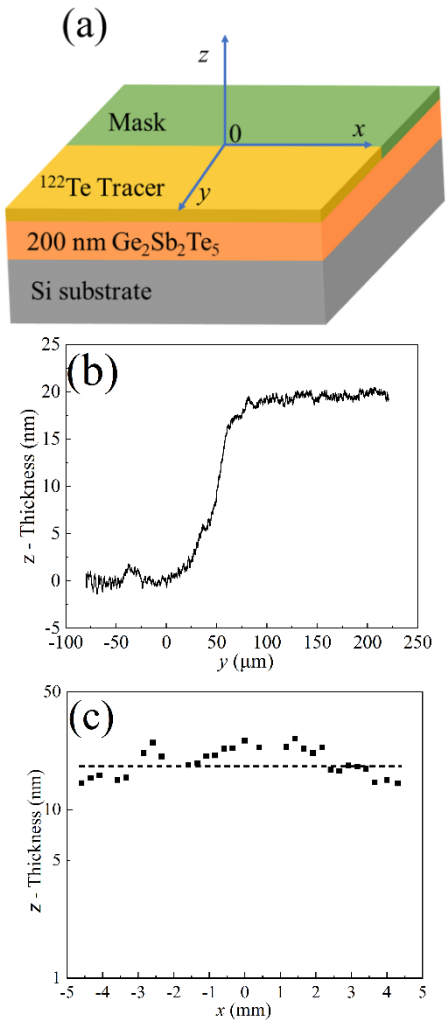

Fig. 1(a) Schematic diagram of the diffusion samples; (b) ^{122}Te thickness along the *y* axis; (c) ^{122}Te thickness along the *x* axis.

The ^{122}Te penetration profiles were measured by ToF-SIMS (IONTOF "TOF.SIMS^5-300"). This technique is highly sensitive and provides information on the atomic and molecular composition with nanometer depth resolution and with sensitivities at the ppm level and a lateral resolution down to about 100 nm. The final depth of each sputter crater formed during the ToF-SIMS measurement was analyzed with an optical profiler (Sensofar plu Neox) in order to establish a depth scale for evaluating the erosion rate during the analyses. In ToF-SIMS, two different ion beams were used for data acquisition. A so-called sputter beam of Cs^+ (500 eV) was employed to erode the specimen meanwhile a second ion beam of Bi_3^+ (25 keV) was applied for the chemical characterization of the resulting crater bottom. The data was acquired from an area of 100 × 100 μm^2, which was chosen from an area larger than 200 × 200 μm^2 without any visible defects.

Table 1 ^{122}Te self-diffusion coefficients, *D* (m/s^2), in GST thin films measured at different temperatures.

Tracer	Temperature (K)	Annealing Time (s)	Diffusion Coefficients (10^{-22} m/s^2)
^{122}Te	291	2592000	0.0140 ± 0.0078)
	320	25200	2.70 ± 0.55
	333	14400	18.2 ± 1.2
	343	3600	38.3 ± 4.0
	353	420	459 ± 400

3. Results and Discussion

3.1 Microstructure and chemical homogeneity

As can be seen from the XRD patterns in Fig. 2(a), after deposition, the sample is completely X-ray amorphous as reflected by the two weak and broad peaks at $2\theta = 28.5°$ and $2\theta = 48°$. XRD scans for samples after different isothermal annealing steps are provided in Fig. 2(b-f). The as-deposited materials were annealed under the same conditions as for the heat treatments of the diffusion annealing, and the corresponding annealing temperatures and times are denoted in figures. In each case, the thickness of the thin GST films was about 200 nm. For the XRD measurements, 200 nm is not thick enough to only detect the signal of the GST layer. Therefore, the peak of the single-crystalline Si substrate at 69° is also visible in Fig. 2(b-f). For comparison, the XRD patterns of the diffusion samples ^{122}Te/GST/Si after different heat treatments are also shown in Fig. 2(b-f). An analysis of the emerging new peaks identifies

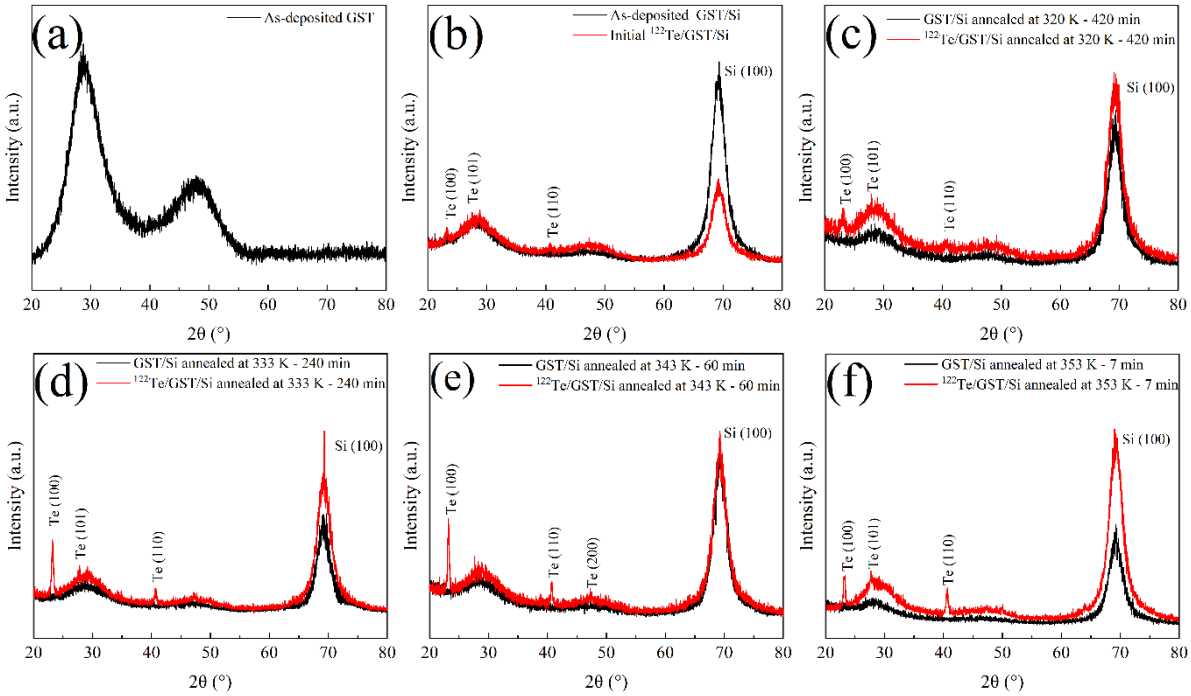

Fig. 2 XRD patterns of (a) as-deposited GST thin films; (b)-(f) GST/Si and ^{122}Te/GST/Si after diffusion heat treatment. The annealing temperatures and times are 320 K - 420 min, 333 K - 240 min, 343 K - 60 min, 353 K -7 min, respectively, which are identical to the conditions of the diffusion heat treatment. The sample ^{122}Te/GST/Si without diffusion heat treatment is shown as "initial" diffusion sample.

those to derive from the pure ^{122}Te.

The weak and broad peaks observed on the annealed samples indicate that annealing up to 353 K did not change the amorphous state of GST thin films. Thus, the thermal treatment for diffusion does not induce crystallization, and the combination of these results pre-confirms that all subsequent diffusion measurements were carried out on the amorphous state.

AFM images of as-deposited GST films with a thickness about 200 nm are shown in Fig. 3. The film features a very smooth surface morphology and exhibits an average roughness of about 1 nm. Compared to the intended diffusion length, $\sqrt{4Dt}$, which is of the order of 4-11 nm, the surface roughness does not influence the measurement of the ^{122}Te diffusion profiles significantly.

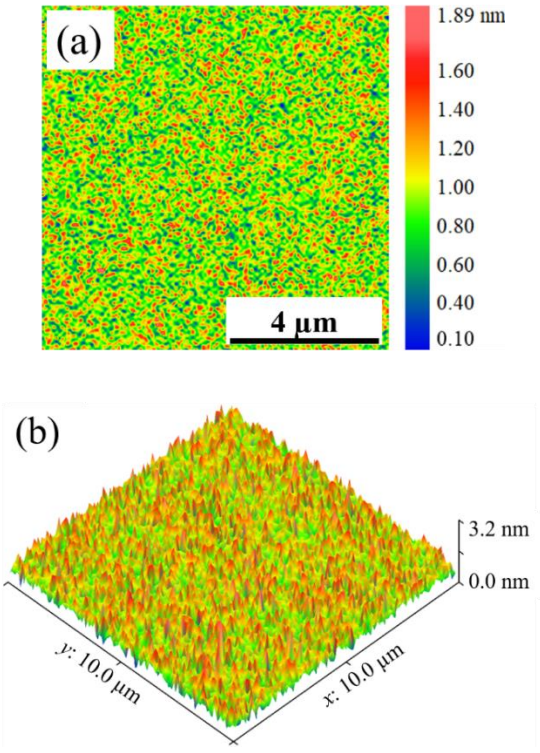

Fig. 3 AFM surface topography of as-deposited GST thin films (a) 2-Dimension, and the corresponding (b) 3-Dimension.

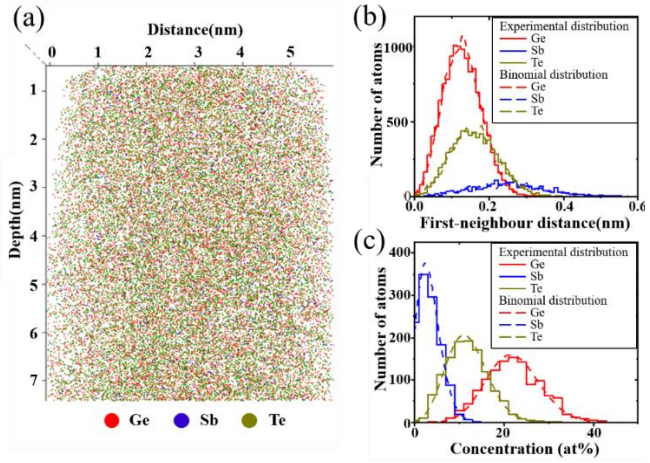

Fig. 4 APT measurements: (a) side view of a volume from the GST sample (red, blue, and dark-yellow dots for Ge, Sb, and Te atoms, respectively); (b) distributions of Ge-Ge, Sb-Sb, and Te-Te first-neighbor distances and (c) concentration distributions of single Ge, Sb, and Te atoms measured in the volume presented in (a).

The brittleness of the material, especially at the ^{122}Te/GST and GST/Si interfaces, did not allow the measurement of the ^{122}Te diffusion profile by APT, and only relatively small APT volumes, see Fig. 4(a), could be acquired before the sample fractured. However, the alloy composition and the atomic distributions were reliably determined. Fig. 4(a) presents the results obtained from a single APT volume, which are representative of the data analyzed from five volumes collected at different depths in the sample (Figs. 4(a) and 6(f)). Fig. 4(b) presents the distributions of Ge-Ge, Sb-Sb, and Te-Te first-neighbor distances in the alloy, which are found to be in good agreement with the theoretical binomial laws. A single average distance is found for each element of the alloy, which excludes the existence of clusters, since otherwise two distances would be observed, one distance for the matrix atoms and one for the cluster atoms. Although the interatomic distances found by APT should not be considered quantitatively, one can safely conclude that Ge and Sb exhibit similar average first-neighbor distances below 0.2 nm and the Te atoms exhibit an average first-neighbor distance above 0.2 nm. Fig. 4(c) shows the concentration distributions of Ge, Sb, and Te detected as single atoms. Furthermore, several molecular types were detected, GeTe, SbTe, and Sb_2Te. The results confirm that all elements or molecules are randomly distributed in the GST alloy without any clustering.

3.2 Tracer diffusion measurements

As demonstrated above, all diffusion experiments were carried out in the amorphous GST phase. The ^{122}Te concentration-depth profiles in GST for all diffusion samples obtained by ToF-SIMS are shown in Fig. 5a. In each case, the ^{122}Te intensity is normalized to the corresponding ^{128}Te intensity, which is the most abundant isotope in GST and which is abbreviated as Te in this paper, to account for variations of the sputtering yield. The normalized intensity, ^{122}Te/Te, vs. the diffusion depth, x, was found to be fitted well by the following equation,

$$C(x,t) = \underbrace{C_1 * erfc\left(\frac{x-x_1}{2\omega_1}\right)}_{\text{remnant 122-Te layer}} + \underbrace{C_2 * erfc\left(\frac{x-x_2}{2\omega_2}\right)}_{\text{Te-rich GST layer}} + \underbrace{C_0 * \exp\left(-\frac{(x-x_0)^2}{4b^2}\right)}_{\text{tracer diffusion}} + \underbrace{C_b}_{\text{background}} \quad (2)$$

Here, $C(x,t)$ is the concentration at the depth x from the surface after the annealing time t; x_i, C_i $(i = 0,1,2)$, b, ω_1, ω_2 are fitting parameters; C_b is the background value corresponding to a natural abundance of the ^{122}Te isotope in natural Te illustrated by the orange dashed lines in Fig. 5 (b); and erfc(z) is the so-called complementary error function. The fitting results for the initial profiles and for a profile

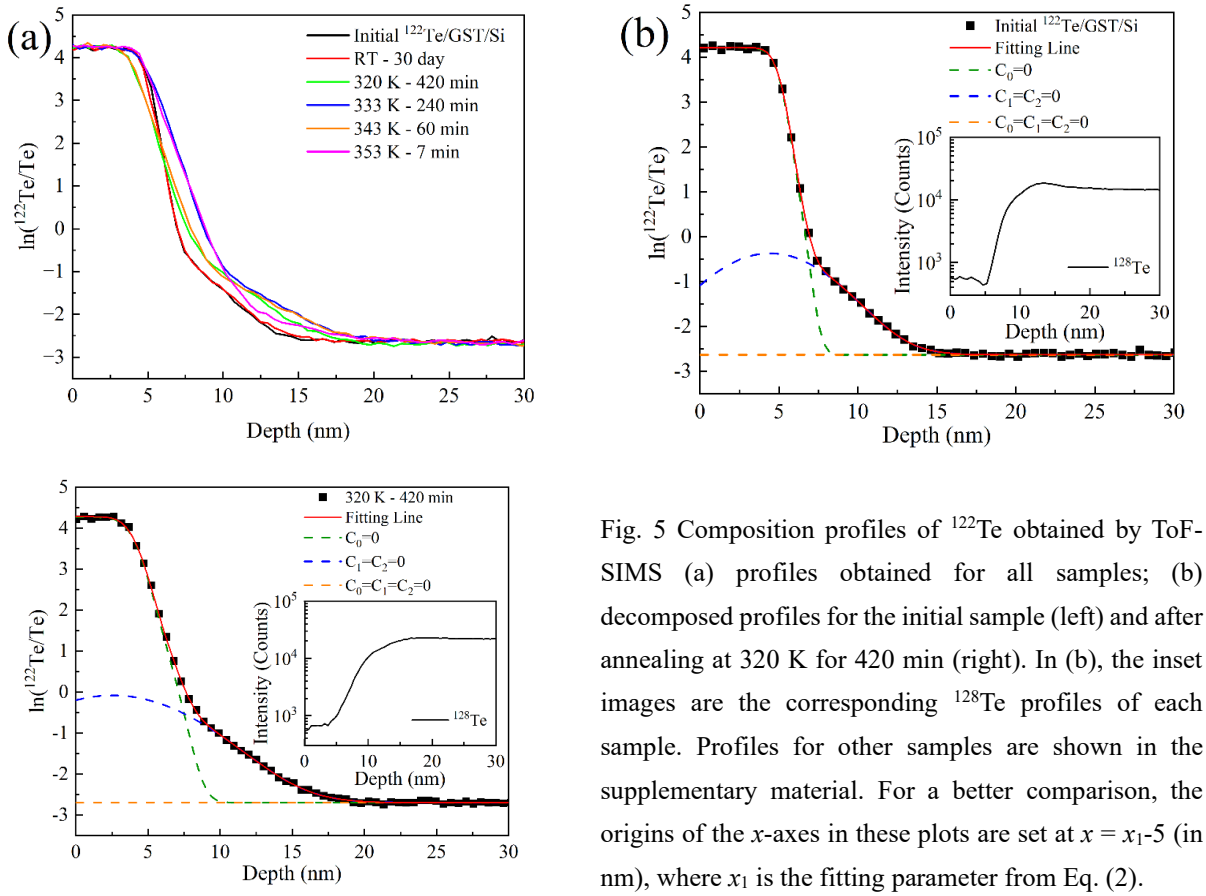

Fig. 5 Composition profiles of ^{122}Te obtained by ToF-SIMS (a) profiles obtained for all samples; (b) decomposed profiles for the initial sample (left) and after annealing at 320 K for 420 min (right). In (b), the inset images are the corresponding ^{128}Te profiles of each sample. Profiles for other samples are shown in the supplementary material. For a better comparison, the origins of the *x*-axes in these plots are set at $x = x_1$-5 (in nm), where x_1 is the fitting parameter from Eq. (2).

obtained after annealing at 320 K for 420 min are shown in Fig. 5 (b) as examples. Note that the origin of the depth coordinate in Fig. 5 is defined as x_1−5 (in nm). Additional profiles are given in the supplementary material. An initial diffusion sample was taken into consideration as a reference to extract the influence of the deposition process itself.

The shape of the concentration profiles and the chosen fit functions are explained by (i) the remnant contribution of an almost pure ^{122}Te layer (x_1, C_1, ω_1); (ii) formation of a Te-rich GST layer (x_2, C_2, ω_2) resulting from mixing of ^{122}Te and GST matrix atoms during PVD-deposition; (iii) diffusion of the ^{122}Te atoms in the GST matrix and (iv) a natural background for the stable ^{122}Te isotope. The combined contribution of the first two terms, (i) and (ii), is indicated by green dashed lines in Fig. 5 (b). Note that annealing-induced modifications of this contribution, given by the erfc terms, correspond to chemical interdiffusion between the Te-rich layer and the GST matrix which is not considered in the present study, since a correct/full thermodynamic description of the Ge-Sb-Te system would be required. Here, we are interested in *true tracer diffusion* of Te in GST which is accounted by the term (iii) in Eq. (2) represented by a Gaussian function.

A certain penetration of the ^{122}Te isotope in the GST matrix is observed already after sample preparation in as-deposited state, Fig. 5(b), left panel, blue dashed line. Most likely, this branch is influenced by a certain heating of the sample during PVD deposition. Note that XRD study confirmed amorphous state of the GST matrix after ^{122}Te deposition, thus the deposition-induced heating is moderate. Subsequent annealing-induced diffusion results in broadening of this branch, Fig. 5(b), right panel,

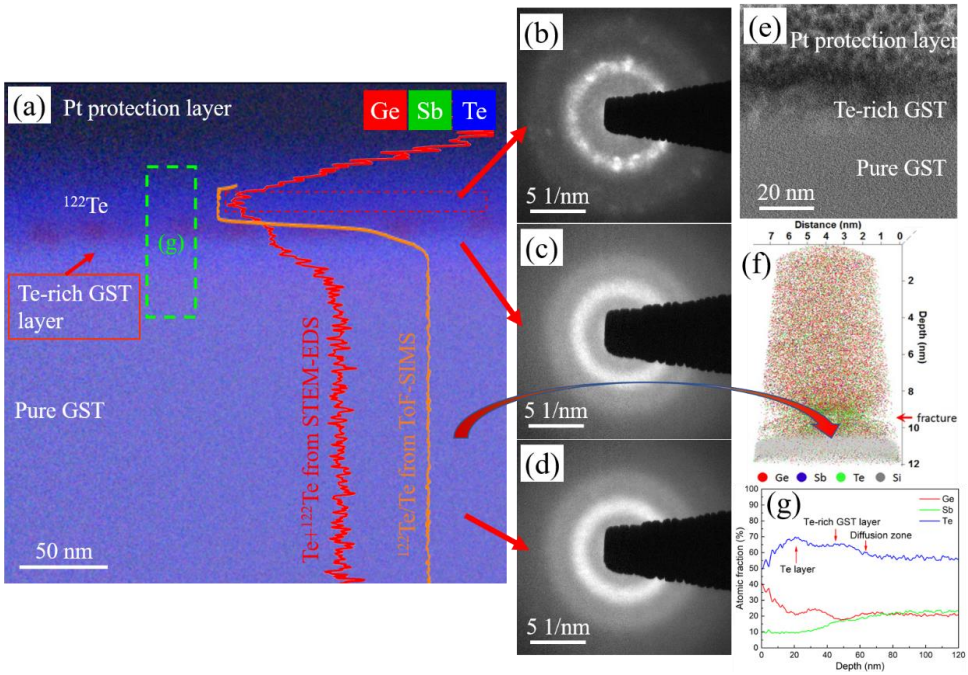

Fig. 6 Elemental distribution and structure characterization of the initial diffusion sample. (a) STEM-EDS map with overlaid ToF-SIMS profiles, (b–d) NBDPs for the diffusion sample ^{122}Te/GST in the selected areas, (e) HAADF image at the ^{122}Te/GST interface, and (f) APT volume analyzed at the bottom of the amorphous film at the GST/Si interface, (g) atomic fraction of ^{122}Te/GST detected by STEM-EDS from the diffusion zone marked by the dashed-green rectangle in (a). A Pt-protection layer was deposited on top of the ^{122}Te isotope.

blue dashed line. This contribution originates from diffusion of the ^{122}Te atoms incorporated in the GST film after ^{122}Te deposition. The branch is adequately described by the Gaussian function and correspond to a dilute limit of Te diffusion in the GST layer. The diffusion coefficients, D, are determined as $D = (b^2 - b_0^2)/t$, where b_0 and b are the corresponding fit parameters, see Eq. (2), for the as-deposited sample (b_0) and that after a diffusion heat-treatment (b) at a constant temperature for a time t, respectively. The results are listed in Table 1. The numerical values of all fitting parameters are indicated in the supplementary material.

The structure and chemical changes induced by Te deposition and diffusion in the GST film were examined further in TEM using STEM-EDS, Fig. 6(a). The cross-sectional chemical map of the heat-treated ^{122}Te/GST sample shows the presence of three clearly distinguished zones. The map is overlaid with the results of a STEM-EDS line scan with respect to the total Te concentration (red line) and the ^{122}Te ToF-SIMS line profile (orange line). A good agreement of the two independent data sets stemming from ToF-SIMS analysis and TEM examination is found.

NBDPs were recorded at characteristic positions in the vicinity of the ^{122}Te/GST interface, Fig. 6 (b)-(d). A nanocrystalline state of the upper ^{122}Te layer is evident from Fig. 6 (b). Below the top metallic ^{122}Te layer, two dissimilar regions in the GST film are distinguished. The first, just beneath the Te layer, is recognized as a Te-rich GST layer produced by ^{122}Te mixing with GST during ^{122}Te deposition. This layer reveals a bright contrast in the high angle annular dark field (HAADF) signal Fig.6 (e) with respect to

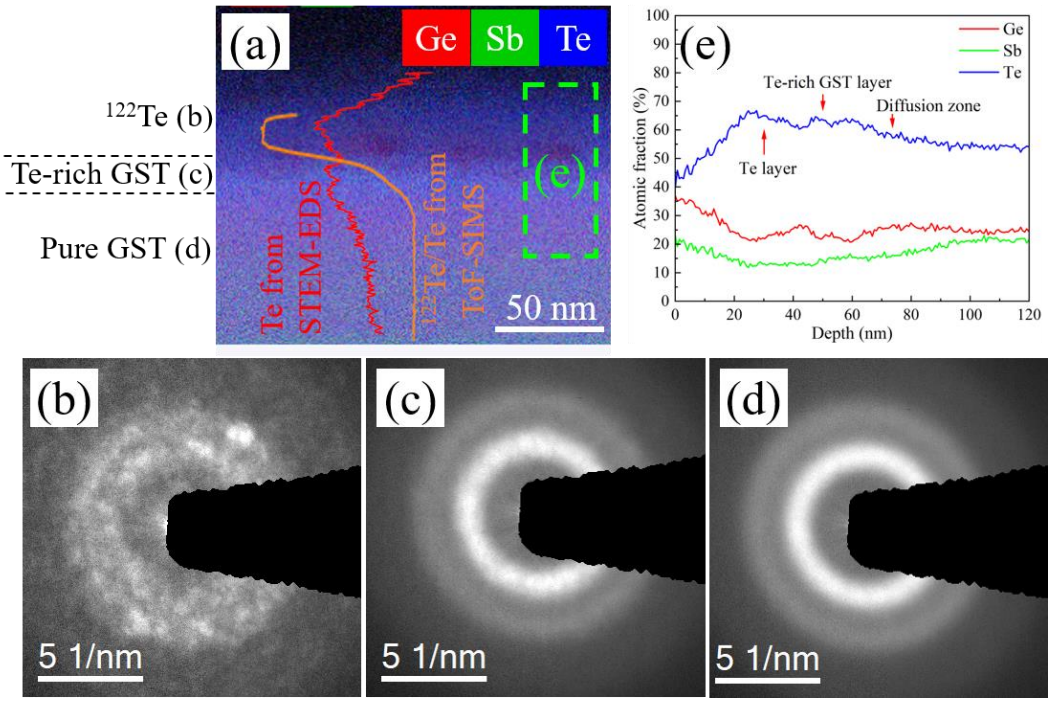

Fig. 7 Elemental distribution and structure characterization of the diffusion sample Te/GST annealed at 320 K - 420 min. (a) STEM-EDS map with overlaid ToF-SIMS profiles (orange line) and Te chemical composition (red line), (b-d) NBDPs for the diffusion sample ^{122}Te/GST in the selected areas, (e) atomic fraction of ^{122}Te/GST detected by STEM-EDS in the diffusion area from the dashed-green rectangle and marked "e" in (a).

the deeper GST film. This area corresponds to a sharp decrease of the ^{122}Te intensity measured by ToF-SIMS, Fig. 6 (a), the Te atomic fraction increased and reached the maximum value since the signal is the sum of Te and ^{122}Te detected by STEM-EDS, Fig. 6(g). Additionally, diffusion broadened this Te-rich GST layer. At larger depth, the atomic ratio of Te become constant. At the same time, the ^{122}Te intensity continuously decreased to a minimum, namely the background, which indicates the presence of the original GST layer. Also, the NBDPs in Fig. 6 (c, d) represent distinctly amorphous phases, verifying that no crystallization was induced by the employed deposition, except leading to a Te-rich GST layer. The TEM results also reveal that diffusion, at least the contribution from the first term in Eq. (2), is driven by a concentration gradient. In Fig. 6(g), an increase of the Ge concentration in the ^{122}Te layer is observed for depths less than 10 nm. This feature might be induced by Ge atom migration into the top pure ^{122}Te layer from the Te-rich GST layer during late stages of ^{122}Te deposition and/or the diffusion heat treatments. However, the measured concentration of Ge in the diffusion zone is very close to that in pure GST. Therefore, the Ge content in the top "pure" Te layer did not affect the reliability of our Te-diffusion measurements and is out of scope of the present study.

Structure changes induced by diffusion heat treatment were investigated by STEM-EDS and NBDPs on the diffusion sample Te/GST annealed at 320 K in Fig. 7. The cross-sectional chemical map also shows three visible zones that are the same as the initial sample. As a consequence of further diffusion heat treatments, the Te-rich GST layer was broader than in the

initial sample. In Fig. 7(a), the overlaid Te atomic fraction (red line) collected from STEM-EDS is in good agreement with the result from ToF-SIMS (orange line). Additionally, NBDPs display amorphous structures in Fig. 7(c, d) which correspond to the Te-rich GST and the pure GST layers respectively. Fig. 7(b) indicates the presence of a crystalline structure of metallic ^{122}Te top layer. These results prove that no crystallization of the GST material was induced by the diffusion heat treatments.

ToF-SIMS profiles for all measured samples (in Fig. 5(a)) show that diffusion occurred in a very local area, about 10 nm thick, below the Te-rich GST layer. Elemental mappings of Ge, Sb and Te are displayed in Fig. 6(a) and Fig. 7(a), showing a homogeneous elemental distribution in the pure GST layer. On the STEM-EDS map close to the diffusion zone, it can be evaluated that the chemical composition (in at.%) of the pure GST layer is Ge: Sb: Te = 21.2: 23.2: 55.5 for the initial sample (shown in Fig. 6(g)) and 24.8: 21.6: 53.6 for the sample after diffusion annealing at 320 K for 420 min (in Fig. 7(e)). Thus, within the uncertainty limits of the method, it is safe to perform the diffusion analysis under the assumption of a fixed chemical composition of the GST material.

The temperature dependence of the measured tracer diffusion coefficients, D, in amorphous GST thin films is shown in Fig. 8 and it was found to follow an Arrhenius dependence,

$$D = D_0 \exp\left(-\frac{Q}{RT}\right) \qquad (2)$$

where D_0 is the pre-exponential factor, Q is the activation energy, and RT has its usual meaning. The pre-exponential factor, D_0, is determined as $(5.3^{+110}_{-5.1})$ m^2/s. In the temperature range of 290 K to 355 K, the activation energy, Q, for Te diffusion is obtained as (1.43 ± 0.08) eV.

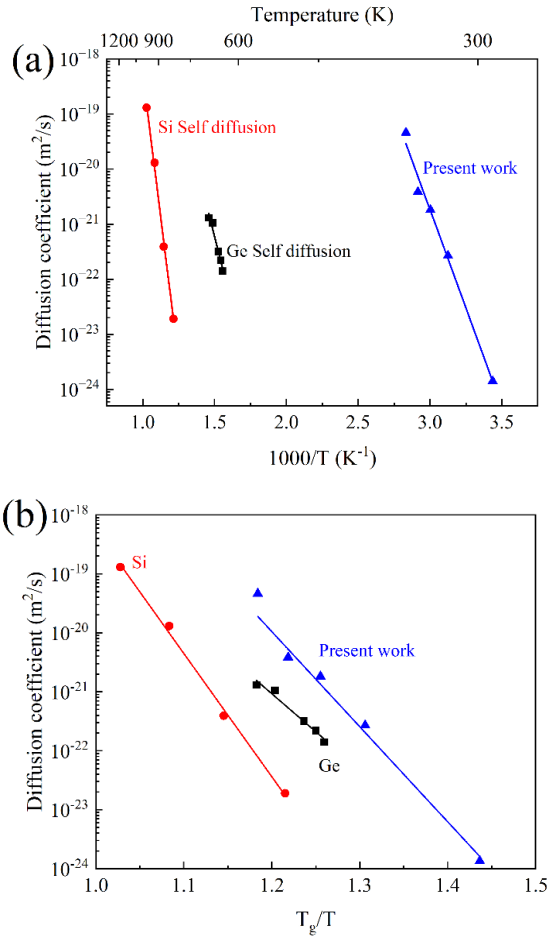

Fig. 8 Temperature dependence of Te self-diffusion into amorphous GST determined in this work (triangle and blue line) in comparison to the self-diffusion rates in amorphous Si [31] (circle and red line) and amorphous Ge [32] (square and black line) are shown. The diffusion coefficients are plotted as functions of the inverse absolute (a) and inverse T_g (b) temperature scales, with T_g being the glass transition temperatures of the corresponding materials.

3.3 Diffusion in phase change materials

In the literature, diffusion in PCMs was scarcely measured. In Fig. 8, the evaluated Te self-diffusion coefficients in amorphous GST are compared with those in different relevant systems. From one side, amorphous Ge and Si can be considered as classical prototypes of amorphous semiconductors having wide applications in optics, energy conversion and in

data storage technology over the last four decades [33–35]. Additionally, amorphous GST, Ge and Si, have typical features of disordered p-type semiconductors [36–38] and they have covalent bonds in the amorphous state. In Fig. 8(b), the diffusivities normalized on the corresponding glass transition temperatures, T_g, are shown [39,40].

Compared with the inverse homologous temperature scale, in Fig. 8(b), Te self-diffusion in the GST system is significantly faster than those for the other two systems in the same range of normalized temperatures. This obvious difference is essentially ascribed to the lower activation energy of 1.43 eV in amorphous GST compared to amorphous Si: 4.4 eV [31] and amorphous Ge: 2.1 eV [32], as shown in Table 2.

In the context of the activation energy for self-diffusion, a comparison with the data provided in the literature from analyzing the activation energy for crystallization of amorphous GST should be shortly discussed. Those data obtained on the phase transformation has often been obtained in a macroscopically averaging way by applying differential scanning calorimetry or in-situ electrical resistance measurements, respectively [41–43]. According to the literature, activation energies in the range of 2.0 to 2.5 eV were evaluated. Compared to the activation energy for self-diffusion, as obtained in the present work by direct diffusion measurements, a large discrepancy of the order of a factor of 2 is found. However, one should keep in mind that these values are not directly comparable and do not necessarily describe the activation of the same underlying processes. In fact, as Te can be seen as representing average diffusion behavior of the constituting elements in GST, the remarkable difference between the activation energy for self-diffusion and the value obtained indirectly by analyzing the rate dependence of the crystallization process indicates that crystallization is most probably not based on single-atom attachment kinetics. As the observed activation energy values for crystallization are significantly larger, it is expected that more complex nucleation and growth modes are involved, possibly involving the rearrangement of groups of atoms or motifs to form crystalline aggregates.

As indicated in the literature, the activation energies for diffusion in amorphous Si and Ge are the sum of a defect formation and a migration part [31,32,44]. Compared to self-diffusion in other glasses, the activation energy obtained for the amorphous GST in the present work is quite low. In covalent glasses, the existence of point defects is well established. In the literature, the data on activation energies for diffusion in amorphous covalently bonded materials is limited. The determined activation energy of 1.34 eV in this work is in agreement with the value of 1.76 eV obtained from the Arrhenius dependence of the viscosity of GST measured in the temperature range 333 - 373 K (below T_g) [45]. The activation energy for Te self-diffusion in Te single crystals was determined as 1.53 eV, indicating that self-diffusion in crystalline Te occurs by vacancy migration [46]. For crystalline GST, the energy barrier for vacancy-element migration is estimated to be around 0.8 -1.0 eV by density functional theory (DFT) simulations using the nudged elastic band method [47]. This value is expected to be lower for amorphous GST due to the more open structure. It is therefore expected that the activation energy for diffusion in amorphous GST should also consist of a migration- and a defect formation part. A relatively small fraction of the diffusion activation energy might be related to an increased collectivity of atomic jumps in amorphous GST and excess volume delocalization in the structure.

Table 2 Activation energy Q and pre-exponential factor D_0 of the systems discussed in the present work.

Tracer	Alloys	Q (eV)	D_0(m/s^2)	Ref.
^{122}Te	$Ge_2Sb_2Te_5$	1.43±0.08	$5.3^{+110}_{-5.1}$	Present work
^{29}Si	Si	4.4	1.5×10^{5}	[31]
^{73}Ge	Ge	2.1	6.2×10^{-6}	[32]

4. Conclusions

For the first time, Te self-diffusion in amorphous GST thin films was measured using ToF-SIMS analyses utilizing a highly enriched ^{122}Te isotope. A homogeneous GST layer was synthesized by magnetron sputtering. The combination of XRD and NBDPs proves that no crystallization was induced by the ^{122}Te deposition or the subsequent diffusion heat treatment. Self-diffusion coefficients between 10^{-24} to $10^{-20}\,m^2/s$ were measured and it was found that they follow an Arrhenius-type dependence between the room temperature and 353 K with an activation energy for Te-self diffusion of (1.43 ± 0.08) eV. Compared to other amorphous systems, the activation energy for Te diffusion in GST is significantly lower, though it becomes similar to those in amorphous Si or Ge when normalized on the respecting glass transition temperature.

Declaration of Competing Interest

The authors declare that they have no known competing financial interests or personal relationships that could have appeared to influence the work reported in this paper.

Acknowledgments

Qingmei Gong would like to thank China Scholarship Council (CSC) for financial support, and also would like to thank Ardavan Makvandi for the lamellae preparation of diffusion samples. Haihong Jiang also would like to acknowledge funding by CSC program.

References

[1] S. Raoux, Phase change materials, Annual Reviww of Materials Research. 39 (2009) 25–48.

[2] M. Wuttig, N. Yamada, Phase-change materials for rewriteable data storage, Nature Materials. 6 (2007) 824–832.

[3] S. Raoux, F. Xiong, M. Wuttig, E. Pop, Phase change materials and phase change memory, MRS Bulletin. 39 (2014) 703–710.

[4] M. Wutting, Structural transformations of Ge 2 Sb 2 Te 5 films studied by electrical resistance measurements, J. Appl. Phys. 874130 (2000) 4130–4134.

[5] M.H.R. Lankhorst, B.W.S.M.M. Ketelaars, R.A.M. Wolters, Low-cost and nanoscale non-volatile memory concept for future silicon chips, Nature Materials. 4 (2005) 347–352.

[6] S. Raoux, W. Wełnic, D. Lelmini, Phase change materials and their application to nonvolatile memories, Chemical Reviews. 110 (2010) 240–267.

[7] J.M. Lee, Y.H. Song, Y. Saito, Y. Sutou, J. Koike, Investigation of a selective switching device using a phase-change material for a 3-dimensional PCRAM array, Journal of the Korean Physical Society. 62 (2013) 1258–1263.

[8] S.R. Ovshinsky, Reversible Electrical Switching Phenomena in Disordered Structures, Physical Review Letters. 21 (1968) 1450–1453.

[9] S.M. Yoon, K.J. Choi, N.Y. Lee, S.Y. Lee, Y.S. Park, B.G. Yu, Nanoscale observations of the operational failure for phase-change-type nonvolatile memory devices using Ge 2 Sb 2 Te 5 chalcogenide thin films, Applied Surface Science. 254 (2007) 316–320.

[10] S. Lee, J.H. Jeong, T.S. Lee, W.M. Kim, B.K. Cheong, A study on the failure mechanism of a phase-change memory in write/erase cycling, IEEE Electron Device Letters. 30 (2009) 448–450.

[11] A. Debunne, K. Virwani, A. Padilla, G.W. Burr, A.J. Kellock, V.R. Deline, R.M. Shelby, B. Jackson, Evidence of Crystallization–Induced Segregation in the Phase Change Material Te-Rich GST, Journal of The Electrochemical Society. 158 (2011) H965.

[12] S. Cecchi, I.L. Garcia, A.M. Mio, E. Zallo, O.A. El

Kheir, R. Calarco, M. Bernasconi, G. Nicotra, S.M.S. Privitera, Crystallization and Electrical Properties of Ge-Rich GeSbTe Alloys, Nanomaterials. 12 (2022).

[13] W. Banerjee, Challenges and applications of emerging nonvolatile memory devices, Electronics (Switzerland). 9 (2020) 1–24.

[14] P. Zuliani, A. Conte, P. Cappelletti, The PCM way for embedded Non Volatile Memories applications, IEEE Symposium on VLSI Circuits, Digest of Technical Papers. 2019-June (2019) T192–T193.

[15] M. Le Gallo, A. Sebastian, An overview of phase-change memory device physics, Journal of Physics D: Applied Physics. 53 (2020) 213002.

[16] T. Nishihara, A. Tsuchino, Y. Tomekawa, H. Kusada, R. Kojima, N. Yamada, Rewritable Triple-Layer Phase-Change Optical Disk Providing 100 Gbyte Capacity, Japanese Journal of Applied Physics. 50 (2011) 062503.

[17] N. Yamada, Origin, secret, and application of the ideal phase-change material GeSbTe, Physica Status Solidi (B) Basic Research. 249 (2012) 1837–1842.

[18] A. V. Kolobov, P. Fons, A.I. Frenkel, A.L. Ankudinov, J. Tominaga, T. Uruga, Understanding the phase-change mechanism of rewritable optical media, Nature Materials. 3 (2004) 703–708.

[19] C. Zambelli, G. Navarro, V. Sousa, I.L. Prejbeanu, L. Perniola, Phase change and magnetic memories for solid-state drive applications, Proceedings of the IEEE. 105 (2017) 1790–1811.

[20] N. Yamada, E. Ohno, K. Nishiuchi, N. Akahira, M. Takao, Rapid-phase transitions of GeTe-Sb2Te3 pseudobinary amorphous thin films for an optical disk memory, Journal of Applied Physics. 69 (1991) 2849–2856.

[21] N. Yamada, T. Matsunaga, Structure of laser-crystallized Ge2Sb2+xTe5 sputtered thin films for use in optical memory, Journal of Applied Physics. 88 (2000) 7020–7028.

[22] N. Yamada, E. Ohno, N. Akahira, K. Nishiuchi, K. Nagata, M. Takao, High speed overwritable phase change optical disk material, Japanese Journal of Applied Physics. 26 (1987) 61–66.

[23] G.C. Sosso, J. Behler, M. Bernasconi, Atomic mobility in the overheated amorphous GeTe compound for phase change memories, Physica Status Solidi (A) Applications and Materials Science. 213 (2016) 329–334.

[24] G.C. Sosso, J. Behler, M. Bernasconi, Breakdown of Stokes-Einstein relation in the supercooled liquid state of phase change materials, Physica Status Solidi (B) Basic Research. 249 (2012) 1880–1885.

[25] S. Wei, C. Persch, M. Stolpe, Z. Evenson, G. Coleman, P. Lucas, M. Wuttig, Violation of the Stokes–Einstein relation in Ge2Sb2Te5, GeTe, Ag4In3Sb67Te26, and Ge15Sb85, and its connection to fast crystallization, Acta Materialia. 195 (2020) 491–500.

[26] T.Y. Yang, I.M. Park, B.J. Kim, Y.C. Joo, Atomic migration in molten and crystalline Ge2 Sb2 Te5 under high electric field, Applied Physics Letters. 95 (2009) 3–5.

[27] S.M.S. Privitera, A.M. Mio, E. Smecca, A. Alberti, W. Zhang, R. Mazzarello, J. Benke, C. Persch, F. La Via, E. Rimini, Structural and electronic transitions in G e2 S b2 T e5 induced by ion irradiation damage, Physical Review B. 94 (2016) 1–8.

[28] H. Search, C. Journals, A. Contact, M. Iopscience, I.P. Address, A.M. Patil, T.A. Manuscript, I.O.P. Publishing, A. Manuscript, A. Manuscript, C.C. By-nc-nd, A. Manuscript, Linear and non-linear optical properties of Ag doped Ge2Sb2Te5 thin films estimated by single transmission spectra, (2017) 0–25.

[29] D. Lencer, M. Salinga, B. Grabowski, T. Hickel, J. Neugebauer, M. Wuttig, A map for phase-change materials, Nature Materials. 7 (2008) 972–977.

[30] M.K. Miller, K.F. Russell, K. Thompson, R. Alvis, D.J. Larson, Review of atom probe FIB-based specimen preparation methods, Microscopy and Microanalysis. 13 (2007) 428–436.

[31] F. Strauß, L. Dörrer, T. Geue, J. Stahn, A. Koutsioubas, S. Mattauch, H. Schmidt, Self-Diffusion in Amorphous Silicon, Physical Review Letters. 116 (2016) 1–6.

[32] E. Hüger, F. Strauß, J. Stahn, J. Deubener, M. Bruns, H. Schmidt, In-situ Measurement of Self-Atom Diffusion in Solids Using Amorphous Germanium as a Model System, Scientific Reports. 8 (2018) 1–8.

[33] Y. An, Y. Tian, C. Wei, Y. Zhang, S. Xiong, J. Feng, Y. Qian, Recent advances and perspectives of 2D silicon: Synthesis and application for energy storage and conversion, Energy Storage Materials. 32 (2020) 115–150.

[34] J.K. Lee, C. Oh, N. Kim, J.Y. Hwang, Y.K. Sun, Rational design of silicon-based composites for high-energy storage devices, Journal of Materials Chemistry A. 4 (2016) 5366–5384.

[35] G.A.N. Connell, R.J. Temkin, W. Paul, Amorphous germanium III. Optical properties, Advances in Physics. 22 (1973) 643–665.

[36] T. Kato, K. Tanaka, Electronic properties of amorphous and crystalline Ge2Sb 2Te5 films, Japanese Journal of Applied Physics, Part 1: Regular Papers and Short Notes and Review Papers. 44 (2005) 7340–7344.

[37] V. Lehmann, S. Ronnebeck, The Physics of Macropore Formation in Low-Doped p-Type Silicon, Journal of The Electrochemical Society. 146 (1999) 2968–2975.

[38] M. Hirose, T. Suzuki, S. Yoshifuji, Y. Osaka, Electrical and optical properties of amorphous germanium, Japanese Journal of Applied Physics. 13 (1974) 40–45.

[39] A. Hedler, S.L. Klaumünzer, W. Wesch, Amorphous silicon exhibits a glass transition, Nature Materials. 3 (2004) 804–809.

[40] L. Sandoval, C. Reina, J. Marian, Formation of Nanotwin Networks during High-Temperature Crystallization of Amorphous Germanium, Scientific Reports. 5 (2015) 1–10.

[41] Y. Choi, M. Jung, Y.K. Lee, Effect of heating rate on the activation energy for crystallization of amorphous Ge2Sb2Te5 thin film, Electrochemical and Solid-State Letters. 12 (2009) 29–31.

[42] H.S. Tae H Jeng, Crystallization behavior of sputter-deposited amorphous Ge2Sb2Te5 thin film, 86 (1999) 19–21.

[43] G. Singh, A. Kaura, M. Mukul, S.K. Tripathi, Electrical, optical, and thermal properties of Sn-doped phase change material Ge2Sb2Te5, Journal of Materials Science. 48 (2013) 299–303.

[44] I. Santos, L.A. Marqués, L. Pelaz, L. Colombo, Elucidating the atomistic mechanisms driving self-diffusion of amorphous Si during annealing, Physical Review B - Condensed Matter and Materials Physics. 83 (2011) 1–4.

[45] J. Kalb, F. Spaepen, T.P. Leervad Pedersen, M. Wuttig, Viscosity and elastic constants of thin films of amorphous Te alloys used for optical data storage, Journal of Applied Physics. 94 (2003) 4908–4912.

[46] M. Werner, H. Mehrer, H. Siethoff, Self-diffusion and antimony diffusion in tellurium, Journal of Physics C: Solid State Physics. 16 (1983) 6185–6195.

[47] B. Zhang, W. Zhang, Z. Shen, Y. Chen, J. Li, S. Zhang, Z. Zhang, M. Wuttig, R. Mazzarello, E. Ma, X. Han, Element-resolved atomic structure imaging of rocksalt Ge2Sb2Te5 phase-change material, Applied Physics Letters. 108 (2016) 1–5.